AGU PUBLICATIONS

JGR

Journal of Geophysical Research: Space Physics

RESEARCH ARTICLE
10.1002/2016JA022400

Special Section:
Big Storms of the Van Allen Probes Era

**Key Points:**
- Radiation belt electrons experienced rapid acceleration up to multi-MeV during 17 March 2015 storm
- Chorus plays an important role in accelerating electrons to multi-MeV near PSD peak location
- Radial diffusion is critical in redistributing electrons and could provide further acceleration

**Supporting Information:**
- Supporting Information S1

**Correspondence to:**
W. Li,
moonli@atmos.ucla.edu

**Citation:**
Li, W., et al. (2016), Radiation belt electron acceleration during the 17 March 2015 geomagnetic storm: Observations and simulations, *J. Geophys. Res. Space Physics*, *121*, 5520–5536, doi:10.1002/2016JA022400.

Received 17 JAN 2016
Accepted 8 JUN 2016
Accepted article online 10 JUN 2016
Published online 30 JUN 2016



# Radiation belt electron acceleration during the 17 March 2015 geomagnetic storm: Observations and simulations

**W. Li[1], Q. Ma[1], R. M. Thorne[1], J. Bortnik[1], X.-J. Zhang[1,2], J. Li[1], D. N. Baker[3], G. D. Reeves[4], H. E. Spence[5], C. A. Kletzing[6], W. S. Kurth[6], G. B. Hospodarsky[6], J. B. Blake[7], J. F. Fennell[7], S. G. Kanekal[8], V. Angelopoulos[2], J. C. Green[9], and J. Goldstein[10,11]**

[1]Department of Atmospheric and Oceanic Sciences, UCLA, Los Angeles, California, USA, [2]Institute of Geophysics and Planetary Physics/Earth, Planetary and Space Sciences, UCLA, Los Angeles, California, USA, [3]Laboratory for Atmospheric and Space Research, University of Colorado Boulder, Boulder, Colorado, USA, [4]Space Science and Applications Group, Los Alamos National Laboratory, Los Alamos, New Mexico, USA, [5]Institute for the Study of Earth, Oceans, and Space, University of New Hampshire, Durham, New Hampshire, USA, [6]Department of Physics and Astronomy, University of Iowa, Iowa City, Iowa, USA, [7]The Aerospace Corporation, Los Angeles, California, USA, [8]NASA Goddard Space Flight Center, Greenbelt, Maryland, USA, [9]Space Hazard Applications, Golden, Colorado, USA, [10]Space Science and Engineering Division, Southwest Research Institute, San Antonio, Texas, USA, [11]Department of Physics and Astronomy, University of Texas at San Antonio, San Antonio, Texas, USA

**Abstract** Various physical processes are known to cause acceleration, loss, and transport of energetic electrons in the Earth's radiation belts, but their quantitative roles in different time and space need further investigation. During the largest storm over the past decade (17 March 2015), relativistic electrons experienced fairly rapid acceleration up to ~7 MeV within 2 days after an initial substantial dropout, as observed by Van Allen Probes. In the present paper, we evaluate the relative roles of various physical processes during the recovery phase of this large storm using a 3-D diffusion simulation. By quantitatively comparing the observed and simulated electron evolution, we found that chorus plays a critical role in accelerating electrons up to several MeV near the developing peak location and produces characteristic flat-top pitch angle distributions. By only including radial diffusion, the simulation underestimates the observed electron acceleration, while radial diffusion plays an important role in redistributing electrons and potentially accelerates them to even higher energies. Moreover, plasmaspheric hiss is found to provide efficient pitch angle scattering losses for hundreds of keV electrons, while its scattering effect on $>1$ MeV electrons is relatively slow. Although an additional loss process is required to fully explain the overestimated electron fluxes at multi-MeV, the combined physical processes of radial diffusion and pitch angle and energy diffusion by chorus and hiss reproduce the observed electron dynamics remarkably well, suggesting that quasi-linear diffusion theory is reasonable to evaluate radiation belt electron dynamics during this big storm.

## 1. Introduction

The Earth's Van Allen radiation belts have a two-zone or one-zone structure depending on electron energy, and these electron fluxes exhibit a dramatic variability particularly during geomagnetically disturbed periods [e.g., *Van Allen*, 1959; *Blake et al.*, 1992; *Li et al.*, 1993; *Fennell et al.*, 2015; *Reeves et al.*, 2015]. This dynamical variation is due to the competition between various acceleration, loss, and transport processes in the radiation belts [*Reeves et al.*, 2003; *Turner et al.*, 2014; *Kanekal et al.*, 2015]. Although major advances have been made on understanding the important physical processes driving radiation belt electron flux variation over the past decade, there still remain outstanding scientific questions, such as (1) when and where each physical mechanism is dominant and (2) what their quantitative roles are in driving radiation belt electron dynamics.

Regarding how electrons are accelerated to ultrarelativistic energies in the radiation belts, several mechanisms have been considered to be potentially important. Although energetic electron injections during substorms or enhanced convection provide seed electrons (from tens of keV to hundreds of keV) [*Miyoshi et al.*, 2003; *Baker and Kanekal,* 2008; *Thorne,* 2010; *Boyd et al.*, 2014; *Dai et al.*, 2014; *Jaynes et al.*, 2015], this process is unlikely to directly lead to the net electron acceleration up to multiple MeV. Inward radial diffusion caused by interaction with Ultra-Low-Frequency (ULF) waves can accelerate electrons to

higher energies [*Hudson et al*., 1999; *Mathie and Mann,* 2000; *Perry et al*., 2005; *Ukhorskiy et al*., 2009], but this process alone is unlikely to account for the observed outer radiation belt electron dynamics which often exhibits growing radial peaks in electron phase space density (PSD) at ultrarelativistic energies in the heart of the radiation belts [*Green and Kivelson,* 2004; *Iles et al*., 2006; *Chen et al*., 2007; *Turner et al*., 2014; *Reeves et al*., 2013; *Thorne et al*., 2013a; *Kanekal et al*., 2015]. This suggests that an internal heating process is operating, and the potential candidates for this local acceleration include energy diffusion by chorus and magnetosonic (MS) waves [e.g., *Summers et al*., 2002; *Horne et al*., 2005a, 2005b, 2007; *Thorne et al*., 2013a; *Ma et al*., 2016]. Specifically, chorus is known to play a critical role in accelerating seed electrons to ultrarelativistic energies in the heart of the outer radiation belt [*Horne and Thorne,* 1998; *Summers et al*., 2002; *Horne et al*., 2005a, 2005b; *Miyoshi et al*., 2013; *Thorne et al*., 2013a; *Reeves et al*., 2013; *Li et al*., 2014; *Tu et al*., 2014]. Moreover, *Horne et al.* [2007] suggested that MS waves can also potentially contribute to accelerate electrons to the approximately MeV range via electron Landau resonance, and MS waves have recently been found to be responsible for forming butterfly pitch angle distributions of electrons in both the inner and outer radiation belts [e.g., *Xiao et al*., 2015; *Li et al*., 2016; *Ma et al*., 2016].

Radiation belt electrons can be lost through two physical processes: (1) they can drift into the dayside magnetopause and be removed from the magnetosphere and (2) they can be precipitated into the dense upper atmosphere and lost due to collisions. Losses to the dayside magnetopause play an important role in driving rapid and dramatic depletions of radiation belt electrons either by direct drift to the boundary with the aid of enhanced outward radial diffusion [*Brautigam and Albert,* 2000; *Miyoshi et al*., 2003; *Shprits et al*., 2006; *Ohtani et al*., 2009; *Matsumura et al*., 2011; *Turner et al*., 2012] or drift shell bifurcation [*Kim et al*., 2008; *Saito et al*., 2010; *Ukhorskiy et al*., 2011]. Moreover, there is growing support for electron precipitation losses into the upper atmosphere due to pitch angle scattering by various magnetospheric waves [e.g., *Thorne,* 2010]. For example, electromagnetic ion cyclotron (EMIC) waves have been shown to provide efficient precipitation losses for ultrarelativistic electrons [*Thorne and Kennel,* 1971; *Summers and Thorne,* 2003; *Li et al*., 2007; *Miyoshi et al*., 2008; *Blum et al*., 2013; *Usanova et al*., 2014]. Furthermore, resonant electron interactions with plasmaspheric hiss are also known to provide pitch angle scattering losses over a broad range of energies with a shorter lifetime of a day or less for lower-energy electrons ($<$~200 keV) but a longer lifetime (~1–100 days) for higher-energy electrons ($>$ ~ 1 MeV) [*Meredith et al*., 2006, 2007; *Thorne et al*., 2013b].

A primary tool used to evaluate wave-particle interactions in the radiation belts is quasi-linear diffusion theory [e.g., *Kennel and Engelmann,* 1966; *Schulz and Lanzerotti,* 1974; *Horne and Thorne,* 1998; *Summers et al*., 2002; *Thorne et al*., 2013a]. Test particle simulations have demonstrated the general validity of using quasi-linear theory to describe the effects of broadband small-amplitude waves on radiation belt electrons [e.g., *Tao et al*., 2011]. Although whether quasi-linear theory can adequately describe electron dynamics for the waves with large amplitudes and discrete structures is still under active research [e.g., *Albert,* 2002; *Bortnik et al*., 2008; *Cattell et al*., 2008; *Furuya et al*., 2008; *Tao et al*., 2012, 2014], recent simulation studies have shown that quasi-linear modeling is able to reproduce the essential features of the observed electron distributions in many events [*Horne et al*., 2005a; *Fok et al*., 2008; *Albert et al*., 2009; *Thorne et al*., 2013a, 2013b; *Li et al*., 2014; *Glauert et al*., 2014; *Tu et al*., 2014; *Zheng et al*., 2014; *Su et al*., 2015].

Since various physical mechanisms for causing acceleration or loss of radiation belt electrons have been identified, these multiple processes need to be combined and assessed as a whole to evaluate whether these known physical processes are sufficient or new physical processes are required to explain the observed electron dynamics. It is important to quantify the roles of each physical mechanism by comparing against unprecedented high-quality electron measurements from multiple satellites. In this paper we quantitatively examine the role of radial diffusion, chorus-driven local acceleration, and pitch angle scattering loss by plasmaspheric hiss using a 3-D diffusion simulation during a rapid electron acceleration event, which occurred during the largest geomagnetic storm (17 March 2015) over the past decade. Section 2 describes the data analysis using multisatellite measurements. The observed dynamics of radiation belt electrons and waves is discussed in section 3, followed by the model description in section 4. Quantitative roles of various physical processes are discussed in section 5 by comparing the observed and simulated electron dynamics. In section 6, we summarize and discuss the principle findings of this study.

## 2. Data Analysis

### 2.1. Van Allen Probes and THEMIS Data Analysis

The Van Allen Probes mission, comprising two identical spacecraft with 5.8 $R_E$ apogee [*Mauk et al*., 2013], has provided high-quality measurements of particle and wave dynamics in the near-equatorial magnetosphere since August 2012. Energetic electron measurements from the Relativistic Electron Proton Telescope (REPT) [*Baker et al*., 2013] and Magnetic Electron Ion Spectrometer (MagEIS) [*Blake et al*., 2013] instruments which form part of the Energetic Particle, Composition, and Thermal Plasma (ECT) Suite [*Spence et al*., 2013] are used to analyze the seed electron populations and radiation belt electron distributions. The Electric and Magnetic Field Instrument Suite and Integrated Science (EMFISIS) provides measurements of DC magnetic fields and a comprehensive set of wave electric and magnetic fields with frequencies from 10 Hz to 12 kHz [*Kletzing et al*., 2013]. Therefore, chorus wave properties with frequencies typically over 0.05–0.8 $f_{ce}$ [*Tsurutani and Smith*, 1977; *Santolík et al*., 2003] can well be evaluated by the EMFISIS Waves instrument, where $f_{ce}$ is electron cyclotron frequency. The High Frequency Receiver (HFR) on EMFISIS provides measurements of the upper hybrid resonance frequency, from which the plasma density can be calculated [*Kurth et al*., 2015].

The multiple THEMIS spacecraft with apogees above 10 $R_E$ [*Angelopoulos*, 2008] provide extensive wave and particle measurements in the near-equatorial magnetosphere. The filter bank (FBK) data provide electric and magnetic field wave intensity from 0.1 Hz to 4 kHz [*Cully et al*., 2008], from which chorus wave amplitudes can be calculated [*Li et al*., 2009]. Although the upper cutoff frequency (~4 kHz) of the wave instrument limits chorus wave measurements to $>$ ~4 $R_E$, THEMIS provides extensive coverage over $4-10$ $R_E$ for chorus waves, which is complementary to the Van Allen Probes measurements ($<6$ $R_E$).

### 2.2. POES Technique to Infer Chorus Wave Intensity

NOAA Polar Orbiting Environmental Satellites (POES) and European Organization for the Exploitation of Meteorological Satellites (MetOp) satellites are polar orbiting Sun synchronous satellites at an altitude of ~800 km with an orbital period of ~100 min. Space Environment Monitor-2 instrument onboard includes the Medium Energy Proton and Electron Detector, which has two electron solid-state detector telescopes that measure electron fluxes in three energy bands ($>$30 keV, $>$ 100 keV, and $>$ 300 keV) [*Evans and Greer*, 2004; *Green*, 2013]. The center of the 0° telescope is approximately outward along the local zenith, whereas the 90° telescope is mounted approximately perpendicular to the 0° telescope.

Recently, *Li et al.* [2013] and *Ni et al.* [2014] have developed a technique to infer chorus wave intensity from the ratios of these two-directional electron measurements (30–100 keV) made by multiple POES/MetOp satellites at the conjugate low altitudes. Details of this technique are described in *Li et al.* [2013] and *Ni et al.* [2014]. The main advantage of this technique is that the multiple POES/MetOp satellites orbiting in a broad L-magnetic local time (MLT) region allow us to monitor the spatiotemporal evolution of chorus wave intensity on a global scale, which cannot be obtained from in situ wave measurements of equatorial satellites alone that are available in the limited L-MLT range.

## 3. Observations of Relativistic Electrons and Waves During 17 March 2015 Storm

Figure 1 shows an overview of the solar wind parameters, geomagnetic indices, and relativistic electron fluxes during the 17 March 2015 geomagnetic storm. The strong interplanetary shock arrived at ~5 UT on 17 March 2015, as indicated by the sudden and substantial increase (the vertical green arrow) in solar wind velocity (Figure 1a) and solar wind dynamic pressure (Figure 1c). The significant increase in solar wind dynamic pressure pushed the magnetopause location at the subsolar point (obtained using an empirical model based on *Shue et al.* [1998]) into ~5 $R_E$. Correspondingly, MeV electrons experienced a substantial dropout (Figures 1h–1j), which might be caused by the strong magnetopause shadowing effect together with the subsequent outward radial diffusion process [e.g., *Shprits et al*., 2006; *Matsumura et al*., 2011; *Turner et al*., 2012], but the actual physical mechanism needs further investigation. Between ~12 and ~24 UT on 17 March 2015, the interplanetary magnetic field (IMF) $B_z$ in geocentric solar magnetospheric (GSM) coordinate was strongly negative, which led to the substantial decrease in *SYM-H* down to about −235 nT (Figure 1e) and strong substorm activity, as indicated by the *AL* index in Figure 1f. After ~0 UT on 18 March 2015, the dynamic pressure became much weaker, and the magnetopause quickly moved out

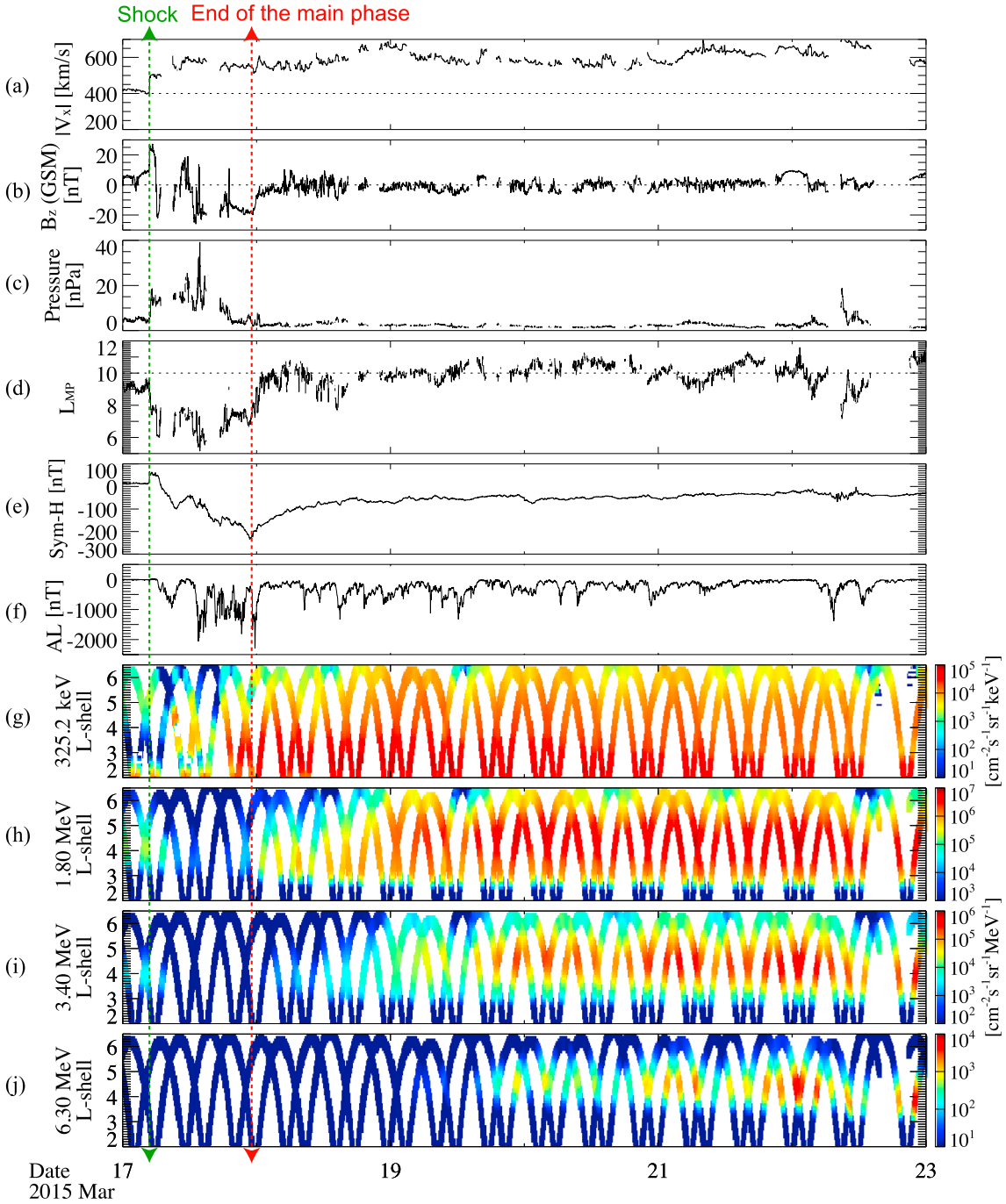


**Figure 1.** An overview plot showing solar wind parameters, geomagnetic indices, and relativistic electron fluxes. (a) Absolute values of solar wind velocity in the Sun-Earth line, (b) interplanetary magnetic field (IMF) $B_z$ in geocentric solar magnetospheric (GSM) coordinate, (c) solar wind dynamic pressure, (d) calculated magnetopause location at the subsolar point based on *Shue et al.* [1998], (e) *SYM-H*, and (f) *AL* index. (g–j) Spin-averaged electron fluxes as functions of time and *L* shell at four different energies. The green and red vertical arrows represent the time of the shock arrival and the end of the storm main phase, respectively.

and varied between ~8 and ~11 $R_E$. During this interval, there was a significant fluctuation in $B_z$, but the mean values remained in the southward direction, which led to frequent substorm-related dips in *AL* (Figure 1f). Southward IMF $B_z$ is known to often cause the enhancement of the relativistic electron fluxes and chorus wave activities [*Miyoshi and Kataoka,* 2008; *McPherron et al.*, 2009; *Li et al.*, 2012; *Miyoshi et al.*, 2013]. From ~0 UT on 18 March 2015 (the vertical red arrow in Figure 1), MeV electrons started to experience acceleration fairly rapidly at lower energies, followed by even higher-energy electrons but with a time delay up to

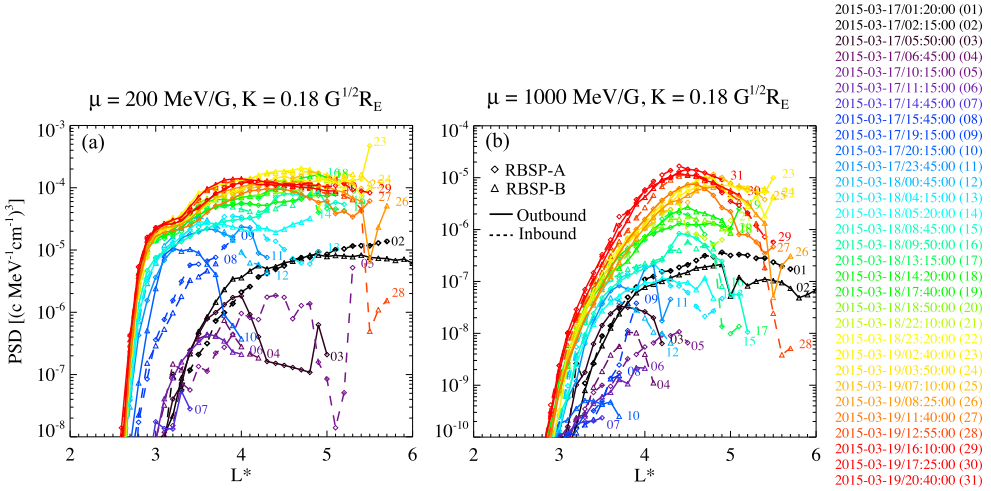


**Figure 2.** (a) Evolution of electron PSD at $\mu = 200$ MeV/G and $K = 0.18\,G^{1/2}\,R_E$ as a function of $L^*$ (TS04D) color coded for different times from early 17 March 2015 to late 19 March 2015. The time indicated on the right side represents the start of the corresponding inbound or outbound pass. Here the diamond and triangle symbols represent the measurements made by Van Allen Probe A and B, respectively, and the outbound (inbound) is shown with solid (dashed) lines. (b) The same as Figure 2a but for $\mu = 1000$ MeV/G and $K = 0.18\,G^{1/2}\,R_E$.

~1.5 days. Another interesting feature is that after 20 March 2015, the peak location of multi-MeV electron fluxes gradually moved to lower $L$ shells. Nevertheless, the "impenetrable barrier" at $L \sim 2.8$ [*Baker et al.*, 2014] was still present for these ultrarelativistic electrons during this large geomagnetic storm.

To evaluate nonadiabatic electron dynamics, electron PSD was calculated as a function of $L^*$ for the fixed first and second adiabatic invariant $\mu$ and $K$ and is shown in Figure 2 from the beginning of 17 March to the end of 19 March (color coded). Here $L^*$ was calculated using the empirical magnetic field model based on *Tsyganenko and Sitnov* [2005]. In association with the shock arrival, electron PSDs at both 200 and 1000 MeV/G substantially decreased and reached the minimum along Orbit 07 starting from ~17 March 2015/14:45 UT. Subsequently, the electron PSD at 200 MeV/G (Figure 2a) increased rapidly, and the accelerated electrons showed a flat or slightly positive radial gradient from early 18 March, suggesting that these seed electrons were primarily transported from higher to lower $L^*$. However, for 1000 MeV/G (Figure 2b) the electron PSD increased gradually starting from Orbit 08, and clear rising peaks in electron PSD were observed in the following orbits, indicating that local heating process was operating for these ultrarelativistic electrons. Since chorus is a potentially important mechanism of causing this local acceleration [e.g., *Summers et al.*, 2002; *Miyoshi et al.*, 2003; *Horne et al.*, 2005a, 2005b; *Reeves et al.*, 2013; *Thorne et al.*, 2013a], we evaluated the global evolution of chorus wave intensity using multisatellite observations.

Figure 3 shows the chorus wave evolution observed by THEMIS and Van Allen Probes, as well as inferred from multiple POES/MetOp satellites. During this event, the apogees of THEMIS and Van Allen Probes were in the afternoon and premidnight sector, respectively, as shown in Figure S1 in the supporting information. As shown in Figure 3c, THEMIS only captured chorus waves over ~4–5 $R_E$ during outbound orbits near the noon sector between 17 March 2015/12 UT and 19 March 2015/16 UT, but the observed chorus wave intensity was very weak in the afternoon and dusk sector. Van Allen Probes captured strong chorus waves mostly during inbounds near the midnight sector from 17 March 2015/09 UT to 19 March 2015/12 UT, while chorus wave intensity was much weaker in the premidnight and dusk sector. Although in situ chorus wave observations from Van Allen Probes and THEMIS were limited during this event, multiple POES/MetOp satellites provide extensive indirect coverage of the chorus wave evolution on a global scale. Figures 3e–3g show inferred chorus wave intensity using the POES technique over 00–04 MLT, 04–08 MLT, and 08–12 MLT. It is reasonable to assume that chorus wave intensity was very weak ($<$ ~10 pT) over 12–24 MLT based on the Van Allen Probes and THEMIS observation, which is also consistent with the statistical distribution of chorus wave intensity [*Li et al.*, 2009, 2011; *Meredith et al.*, 2012]. Figures 3h and 3i show chorus wave intensity averaged over 24 h of MLT with 4 h and 1 h time resolution. The chorus wave intensity was strong particularly at lower $L$ shells (down to $L \sim 2.5$) during the main phase of the storm, but chorus wave activity moved to larger $L$ shells

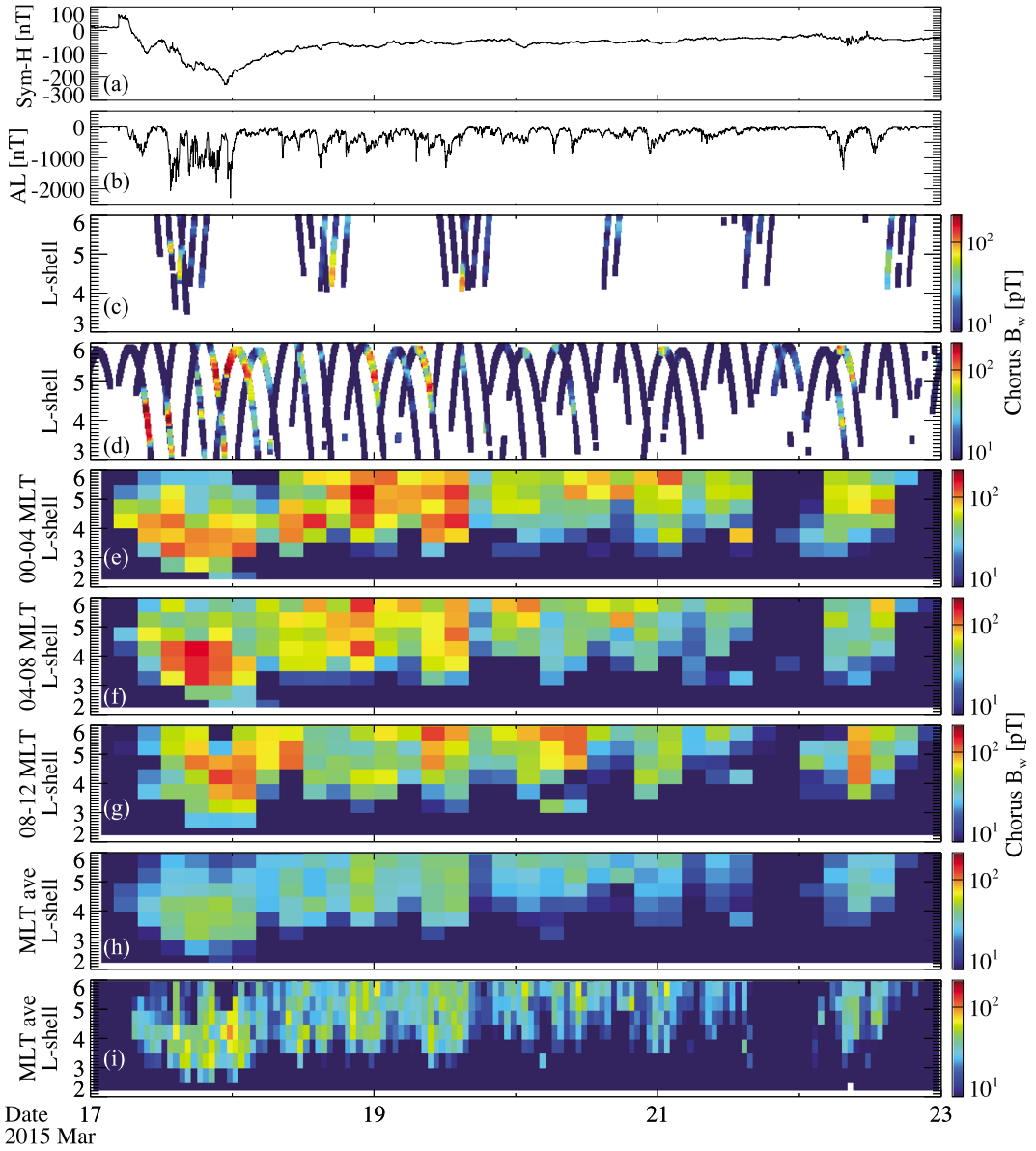


**Figure 3.** Chorus wave evolution using multisatellite observations during the 17 March 2015 geomagnetic storm. (a) *SYM-H*, (b) *AL*, (c) chorus wave amplitudes integrated over 0.05–0.8 $f_{ce}$ using THEMIS FBK wave data, and (d) EMFISIS wave data. (e–g) Inferred chorus wave intensity using the POES technique over 00–04 MLT, 04–08 MLT, and 08–12 MLT. (h) Chorus wave intensity inferred using the POES technique averaged over 24 h of MLT with 4 h time resolution and (i) 1 h time resolution.

from 18 March 2015/00 UT to 19 March 2015/16 UT and became much weaker in the following period. Overall, the evolution of chorus wave activity was generally consistent with the variation of the *AL* index, with larger wave intensity in response to stronger *AL* disturbance [e.g., *Meredith et al*., 2012].

The evolution of electron pitch angle distribution is shown in great detail in Figure 4 (bottom) at $L = 4.5$, where the peak in electron fluxes was observed. Here electron PSD data were collected from both Van Allen Probes A and B when the satellite location satisfied the following criteria: (1) absolute magnetic latitudes less than 5° ($|\mathrm{MLAT}| < 5°$); (2) $L$ shells between 4.45 and 4.55; and (3) ±2 h from the designated time. Subsequently, the collected PSD data were averaged at each local pitch angle and are shown with small diamonds in Figure 4 (bottom). For each PSD data, the corresponding equatorial pitch angle was calculated using the empirical magnetic field model [*Tsyganenko,* 1989], and the fitted PSD profile is shown with the colored lines as a function of equatorial pitch angle. The excellent agreement between the diamonds and

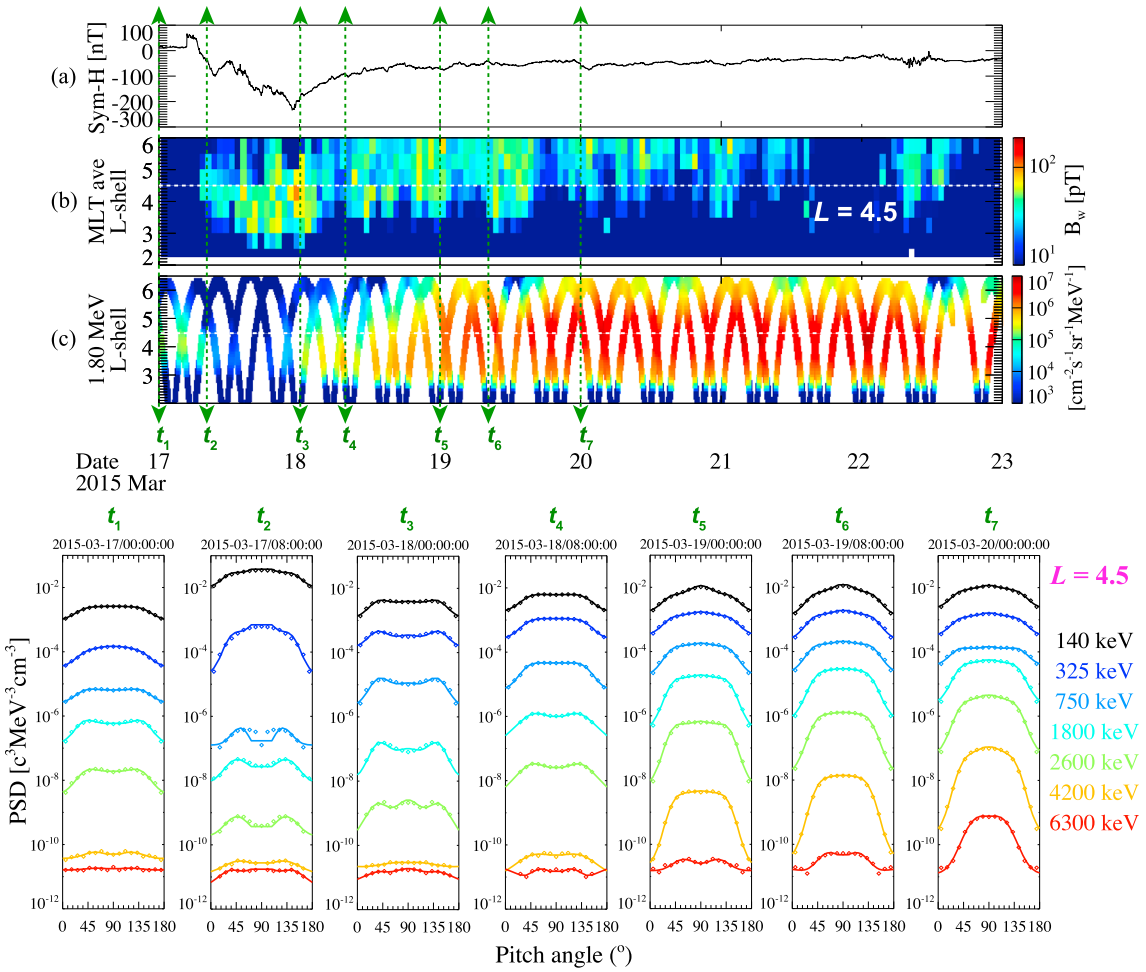


**Figure 4.** (a) *SYM-H* and (b) chorus wave intensity averaged over 24 h of MLT using the POES technique. (c) Time evolution of electron fluxes as a function of *L* shell at 1.8 MeV. The bottom panels show the evolution of electron pitch angle distributions for various electron energies (color coded) at $L = 4.5$ at 7 different times indicated by the green vertical arrows in the top panels. The electron pitch angle distribution data were collected from both Van Allen Probes A and B in the region of $|\mathrm{MLAT}| < 5°$. Each small diamond represents the electron PSD at the measured local pitch angle, and the lines indicate the fitted electron PSD as a function of equatorial pitch angle after mapping using the T89 magnetic field model [*Tsyganenko,* 1989].

lines indicates that near the magnetic equator ($|\mathrm{MLAT}| < 5°$) local and equatorial pitch angles are almost identical. Before the shock arrival ($t_1$), MeV electrons exhibited a modest butterfly pitch angle distribution, which might be caused by the drift shell splitting effect [e.g., *West et al.*, 1973; *Sibeck et al.*, 1987]. At $t_2$, after the substantial increase in solar wind dynamic pressure, >1 MeV electron PSD substantially decreased, and the butterfly distribution became even clearer, which might be caused by the magnetopause shadowing loss followed by the subsequent outward radial diffusion process [*Shprits et al.*, 2006; *Matsumura et al.*, 2011; *Turner et al.*, 2012] at this relatively large *L* shell. In the subsequent time interval (from $t_3$ to $t_7$), MeV electron PSD increased rapidly, and the pitch angle distribution changed from the butterfly distribution to a flat-top distribution, peaking over ~50°–130° with a strong gradient toward the loss cone over pitch angles of 30°–50° and 130°–150°. During this time interval from $t_3$ to $t_7$, when MeV electrons experienced fairly rapid acceleration, MLT-averaged chorus wave intensity was modestly strong (Figure 4b), supporting the scenario that chorus-driven local acceleration may contribute to the observed rapid electron acceleration.

## 4. Model Description

In order to understand the underlying physics causing the observed electron dynamics during this geomagnetic storm, we used a 3-D diffusion code to model the evolution of radiation belt electron dynamics, where

the contribution of each physical process is included in terms of diffusion coefficients. The details of the 3-D diffusion code and diffusion coefficient calculations are described below.

### 4.1. Three-Dimensional Diffusion Code

The evolution of the radiation belt particle PSD due to the radial, pitch angle, and energy diffusion can be described by the modified 3-D Fokker-Planck equation [*Schulz and Lanzerotti*, 1974]:

$$\frac{\partial f}{\partial t} = L^{*2}\frac{\partial}{\partial L^*}\bigg|_{\mu,J}\left(D_{L^*L^*}L^{*-2}\frac{\partial f}{\partial L^*}\bigg|_{\mu,J}\right) + \frac{1}{S(\alpha)sin\ \alpha cos\ \alpha\partial\alpha}\bigg|_{p,L^*}\left(S(\alpha)sin\ \alpha cos\ \alpha\langle D_{\alpha\alpha}\rangle\frac{\partial f}{\partial\alpha}\bigg|_{p,L^*}\right)$$
$$+\frac{1}{S(\alpha)sin\ \alpha cos\ \alpha\partial\alpha}\bigg|_{p,L^*}\left(S(\alpha)sin\ \alpha cos\ \alpha\langle D_{\alpha p}\rangle\frac{\partial f}{\partial p}\bigg|_{L^*,\alpha}\right) + \frac{1}{p^2\partial p}\bigg|_{L^*,\alpha}\left(p^2\langle D_{\alpha p}\rangle\frac{\partial f}{\partial\alpha}\bigg|_{p,L^*}\right)$$
$$+\frac{1}{p^2\partial p}\bigg|_{L^*,\alpha}\left(p^2\langle D_{pp}\rangle\frac{\partial f}{\partial p}\bigg|_{L^*,\alpha}\right) - \frac{f}{\tau}$$

where $f$ is the PSD, $t$ is the time, $\alpha$ is the equatorial pitch angle, and $p$ is the particle momentum. $\mu$ and $J$ are the first and second adiabatic invariants, respectively, and $\langle D_{\alpha\alpha}\rangle$, $\langle D_{pp}\rangle$ and $\langle D_{ap}\rangle$ are the bounce- and drift-averaged diffusion coefficients in pitch angle, momentum, and their mixed terms, and $D_{L^*L^*}$ is the drift-averaged radial diffusion coefficients. $S(\alpha)$ is a function related to the bounce period [*Lenchek et al.*, 1961], and $\tau$ is a quarter of the bounce period (infinity) inside (outside) the bounce loss cone. In this simulation we used a dipole magnetic field model for simplicity, and the relevant discussion on its uncertainty and limitation is given in section 5.

This Fokker-Planck equation is numerically solved using the standard alternating direction implicit method [*Ma et al.*, 2015] and has been fully validated by comparing against previous simulation results using other similar 3-D codes [e.g., *Albert et al.*, 2009; *Shprits et al.*, 2009]. We use this code to evaluate electron PSD evolution for energies corresponding to values of the first adiabatic invariant ($\mu$) from 80 to 22,330 MeV/G, where convection electric field plays an insignificant role in electron dynamics [e.g., *Jordanova and Miyoshi,* 2005; *Shprits et al.*, 2015].

The electron PSD at the inner boundary of $L = 2$ was 0, and the electron PSD at the outer boundary ($L = 6$) was updated every 1 s after interpolating electron measurements by both Van Allen Probes averaged over every 4 h. The electron PSD at the maximum $\mu$ of 22,330 MeV/G was set to zero, and at the minimum $\mu$ of 80 MeV/G was updated every 1 s after interpolating the averaged electron PSD over 4 h derived from both probes to represent the realistic seed electron evolution. Note that the time resolution of the simulated local diffusion processes due to chorus and hiss wave scattering is also 1 s. The PSD at boundaries was updated at every time step (1 s) to avoid the sharp PSD gradients induced by the rapid variations, which could potentially induce unrealistic numerical errors. d$f$/d$\alpha$ is set to zero at $\alpha = 0°$ and $\alpha = 90°$. The grid resolution in $L$ shell and pitch angle is 0.25 and 1°, and ~90 energies were chosen in the logarithmic space. Furthermore, the initial conditions of the electron PSD were derived from the MagEIS and REPT electron measurements on both Van Allen Probes A and B within 2 h around 18 March 2015/00 UT.

### 4.2. Calculation of Diffusion Coefficients

The quantitative effects of radial diffusion, chorus, and hiss on radiation belt electrons are included in the diffusion coefficients. In order to evaluate bounce- and drift-averaged diffusion coefficients driven by chorus, we incorporated chorus wave intensity inferred using the POES technique (as discussed in section 2.2) averaged over each 4 h in different MLT sectors, as shown in Figures 3e–3h. Besides chorus wave intensity, several assumptions were made on chorus wave spectral properties, wave normal distribution, and their latitudinal distribution, which are described in the supporting information Text S1 and Table S1 in detail. In order to incorporate realistic plasma density, we inferred the plasma density from the upper hybrid resonance line of Van Allen Probes EMFISIS data near the nightside. In other MLT sectors, where Van Allen Probes density measurements were unavailable, we scaled the plasma density based on the measured nightside density values using the L-MLT dependent density relation following the empirical plasmatrough density model [*Sheeley et al.*, 2001]. More specifically, the density values ($n_1$) in other MLT sectors ($MLT_1$) are calculated by

$$n_1 = n_0\frac{124\left(\frac{3}{L}\right)^4 + 36\left(\frac{3}{L}\right)^{3.5}cos\left\{\left\{MLT_1 - \left[7.7\left(\frac{3}{L}\right)^2 + 12\right]\right\}\frac{\pi}{12}\right\}}{124\left(\frac{3}{L}\right)^4 + 36\left(\frac{3}{L}\right)^{3.5}cos\left\{\left\{MLT_0 - \left[7.7\left(\frac{3}{L}\right)^2 + 12\right]\right\}\frac{\pi}{12}\right\}},$$

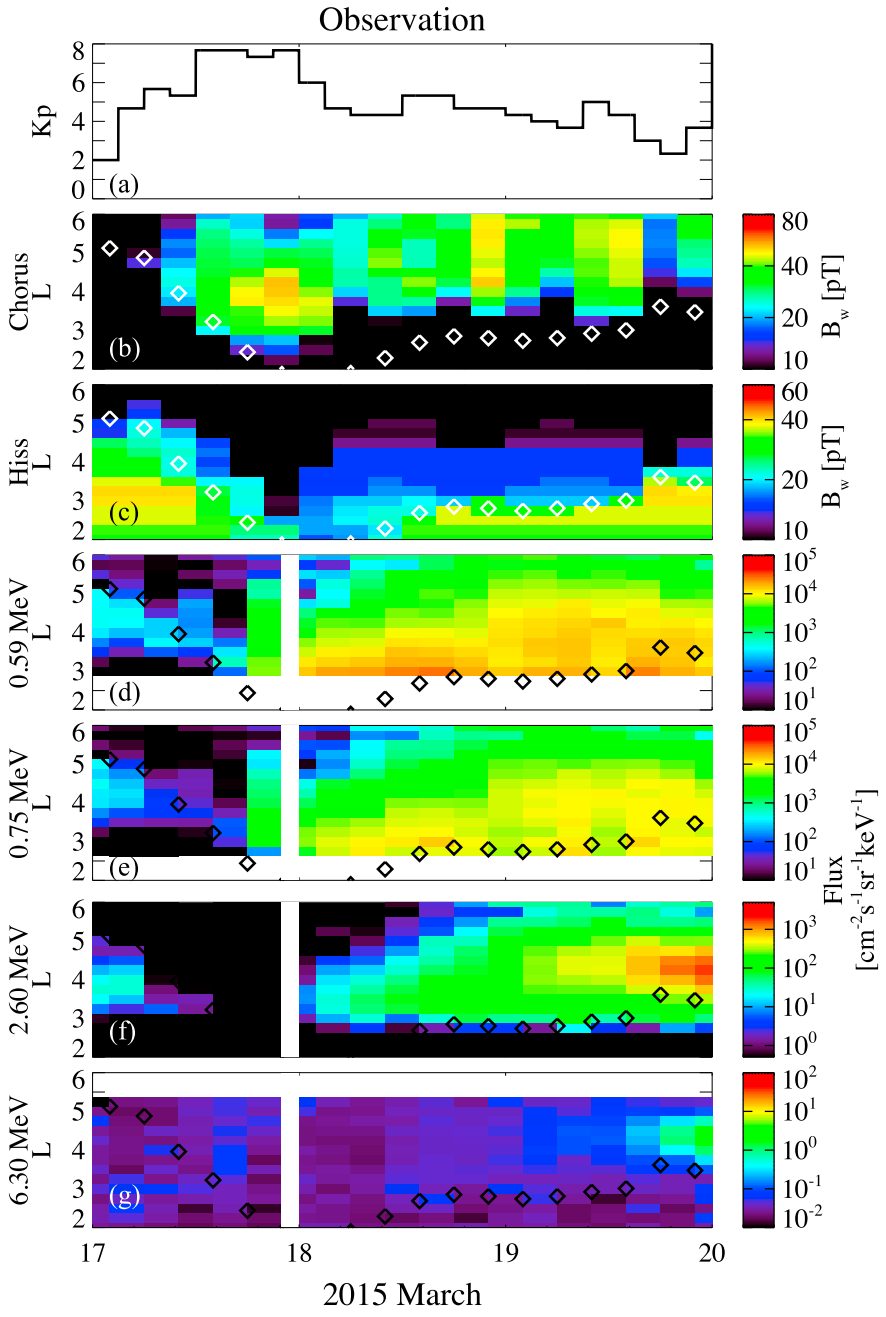


**Figure 5.** (a) *Kp*, (b) chorus wave intensity averaged over 24 h of MLT using the POES technique, and (c) hiss wave intensity averaged over 24 h of MLT using the statistical results [*Li et al.*, 2015a]. (d–g) Electron flux evolution at four different energies. In Figures 5b–5g, each white or black diamond indicates the plasmapause location averaged over 00–12 MLT based on *Goldstein et al.* [2014].

where $n_0$ is the density measured by Van Allen Probes, $L$ and $MLT_0$ are the $L$ shell (in dipole magnetic field) and magnetic local time (in hour) where the Van Allen Probes traversed. The detailed density values are listed in the supporting information Table S2, and the adopted density values are smaller than the empirical density [*Sheeley et al.*, 2001] by a factor of up to ~6 during the period between 18 March 2015/00 UT and 20 March 2015/00 UT. It is important to note that adopting a realistic density model is critical in quantitatively evaluating electron dynamics caused by chorus waves [e.g., *Thorne et al.*, 2013a]. Regarding plasmaspheric hiss, we adopted statistical hiss wave intensity during disturbed geomagnetic activity ($AL^* < -500$ nT) and frequency spectrum according to *Li et al.* [2015a], where $AL^*$ is the minimum $AL$ in the preceding 3 h.

The adopted hiss wave intensity in this simulation is shown in the supporting information Table S3. The wave normal angles of plasmaspheric hiss were assumed to increase with latitudes, with field aligned near the magnetic equator and highly oblique at larger latitudes based on *Ni et al.* [2013]. More importantly, hiss was assumed to be present inside the plasmasphere and plumes. Since the in situ observation of the detailed structure of the plasmasphere and plume is limited, we incorporated the plasmapause location model from *Goldstein et al.* [2014] based on the simulation model that was applied to this event (See supporting information Figure S2). The plasmaspheric plume was present in the afternoon sector in the acceleration interval from $t_3$ to $t_7$. The evolution of chorus and hiss wave intensity averaged over 24 h of MLT is shown in Figures 5b and 5c from 17 to 20 March 2015, followed by the observed electron flux evolution at four different energies (Figures 5d–5g). The plasmapause location averaged over 00–12 MLT based on *Goldstein et al.* [2014] was indicated by the white or black diamonds in Figures 5b–5g. The region where the observed chorus waves were intense is closely related to the movement of the plasmapause location. After constructing the wave and plasma models for chorus and hiss, we calculated bounce- and drift-averaged diffusion coefficients in pitch angle, energy, and their mixed terms, respectively, using the fully validated University of California, Los Angeles (UCLA) Full Diffusion code [e.g., *Ni et al.*, 2008; *Thorne et al.*, 2013a; *Li et al.*, 2014; *Ma et al.*, 2015]. Here we note that a dipole magnetic field model was adopted to calculate diffusion coefficients for simplicity.

In order to calculate radial diffusion coefficients, we adopted two different empirical models from the statistical results: (1) *Brautigam and Albert* [2000] and (2) *Ozeke et al.* [2014]. Both models include radial diffusion caused by electric and magnetic field fluctuations, which are dependent on *Kp* and *L*. We used the radial diffusion coefficients from the sum of fluctuations in electric and magnetic fields to evaluate the total effect of the radial diffusion in radiation belt electron dynamics.

## 5. Comparison of the Observed and Simulated Electron Dynamics

The calculated diffusion coefficients were used as inputs in the 3-D diffusion code to quantitatively evaluate the electron evolution in the recovery phase of the storm from 18 March 2015/00 UT to 20 March 2015/00 UT, when the fairly rapid electron acceleration occurred. In this study, we focus on simulating the acceleration period (recovery phase) rather than the dropout period (main phase) due to the following reason. As shown in Figure 1d, the empirical magnetopause location at the subsolar point moved into ~ 5 $R_E$ during the main phase, and a realistic magnetic field model and 3-D particle tracing code, which can better treat the pitch angle dependent particle drift shell [e.g., *Ukhorskiy et al.*, 2011, 2015], are essential to accurately simulate electron losses toward the magnetopause. However, this is beyond the scope of this paper, and thus, we focus on simulating the acceleration period (recovery phase), when the magnetopause moved out to $> 8\,R_E$.

A detailed comparison between the observed and simulated electron fluxes at 80° pitch angles by including various physical processes is shown in Figure 6 for four different energies. The differences in electron fluxes between the simulation results and the observations are shown in the supporting information Figure S3 to visualize the comparison more quantitatively. By only including radial diffusion based on *Brautigam and Albert* [2000] ($D_{LL}$ (B & A)), the simulated electron fluxes (Figure 6b) are overestimated especially at lower *L* shells (<4) at hundreds of keV compared to the observation (Figure 6a), suggesting that this parameterization of radial diffusion is probably too strong. The simulation result using radial diffusion coefficients from *Ozeke et al.* [2014] ($D_{LL}$ (Ozeke)), as shown in Figure 6c, is more consistent with the observation particularly at lower *L* shells (<3.5), but it clearly underestimates electron flux at middle *L* shells (3.5–4.5). This is consistent with previous studies, which also found that $D_{LL}$ (B & A) is overestimated particularly during active times [e.g., *Huang et al.*, 2010; *Tu et al.*, 2012; *Ozeke et al.*, 2014]. By including chorus-driven local acceleration only, the simulated peak location in electron fluxes (Figure 6d) is roughly consistent with the observation. However, at lower energies of hundreds of keV, the simulated electron fluxes are somewhat overestimated compared to the observation. By including the effect of hiss together with chorus, the simulated electron fluxes (Figure 6e) for hundreds of keV decreased at $L < 4$ due to the pitch angle scattering loss caused by hiss, whereas MeV electron fluxes exhibited an insignificant variation. This is because the hiss-driven electron scattering is more effective for lower energy electrons [*Meredith et al.*, 2006; *Ni et al.*, 2013; *Thorne et al.*, 2013b; *Li et al.*, 2015a]. However, the simulated electron flux peak is narrower compared to the observation, and the simulated electron fluxes are underestimated at $L > 4.5$. By including physical processes of energy and pitch angle diffusion by chorus and

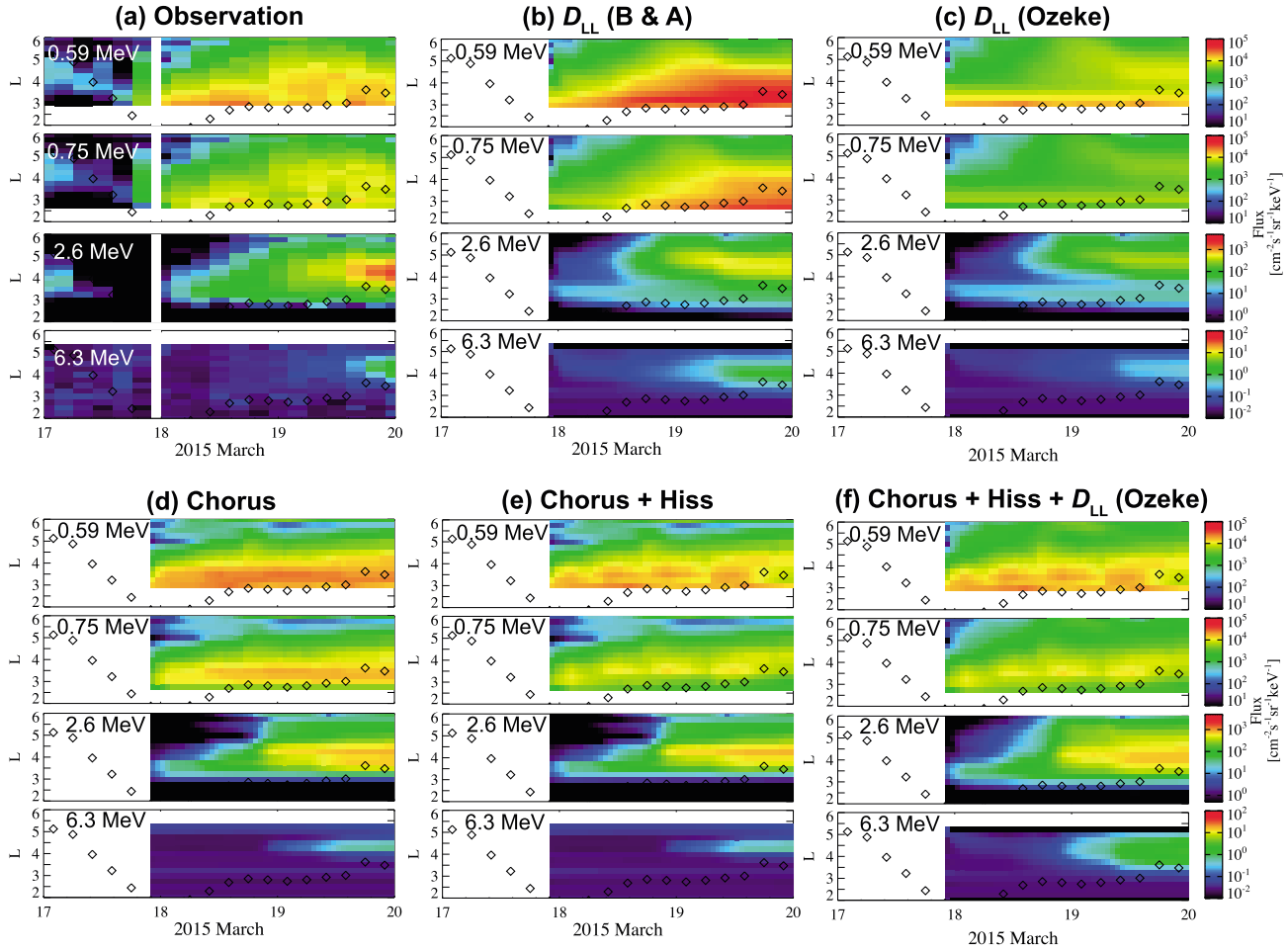


**Figure 6.** Comparison of the observed and simulated electron fluxes. (a) Observed electron fluxes at 80° pitch angles at four different energies, where each black diamond represents the plasmapause location averaged over 00–12 MLT based on *Goldstein et al.* [2014]. (b) Simulated electron flux by only including radial diffusion based on *Brautigam and Albert* [2000], (c) by only including radial diffusion based on *Ozeke et al.* [2014], (d) by only including pitch angle and energy diffusion driven by chorus, (e) by including pitch angle and energy diffusion driven by both chorus and hiss, and (f) by including pitch angle and energy diffusion driven by chorus and hiss, and radial diffusion caused by ULF waves [*Ozeke et al*., 2014].

hiss, as well as radial diffusion based on *Ozeke et al.* [2014] ($D_{LL}$ (Ozeke)), the simulation result (Figure 6f) is most consistent with the observed spatiotemporal evolution of electron fluxes (Figure 6a). Nevertheless, the multi-MeV electron fluxes were still slightly overestimated, and the MeV electron acceleration appeared to develop sooner compared to the observation. This suggests that additional loss processes may be operating for these ultrarelativistic electrons, such as pitch angle scattering by EMIC waves, which is known to be more efficient for MeV electrons [e.g., *Li et al*., 2007; *Miyoshi et al*., 2008; *Blum et al*., 2013; *Omura and Zhao,* 2013; *Usanova et al*., 2014]. The presence of EMIC waves was investigated using in situ wave measurements from THEMIS and Van Allen Probes, and ground-based magnetometers, as well as particle precipitations by POES, and is summarized in the supporting information Figure S4 for both $H^+$ and $He^+$ bands. EMIC waves with modest intensities were observed particularly in the $He^+$ band at $< 4.5\,R_E$ near the afternoon and dusk sector, where EMIC waves are known to be typically effective in causing MeV electron precipitation [e.g., *Millan and Thorne,* 2007; *Jordanova et al*., 2008; *Thorne,* 2010]. However, it is challenging to precisely include EMIC-driven electron precipitation in the simulation because of their complicated wave frequency spectrum and limited measurements in time and space, and thus, it is beyond the scope of this present paper. Nevertheless, the presence of EMIC wave activity shown in Figure S4 supports that an additional loss process may have occurred due to the pitch angle scattering by EMIC waves especially for these ultrarelativistic electrons. Another possibility contributing to the inconsistency between the simulation and observation is the adiabatic effect [e.g., *Kim and Chan*, 1997] due to the difference between the actual magnetic field and the dipole field adopted in our

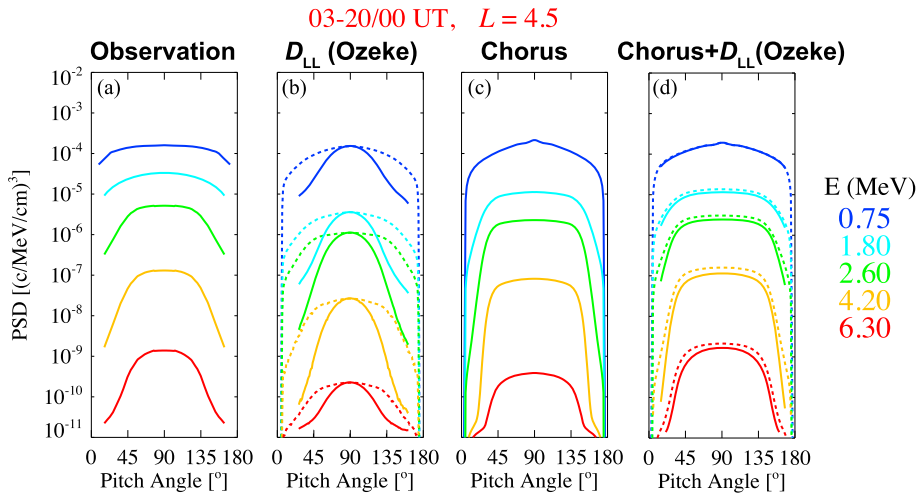


**Figure 7.** Comparison of the observed and simulated electron pitch angle distribution near the end of the simulation period at $L = 4.5$, near the location where the peak in electron fluxes was observed. (a) Observed electron PSD as a function of equatorial pitch angle color coded for various energies, (b) simulated electron pitch angle distribution by including radial diffusion only [*Ozeke et al.*, 2014] (dashed lines) and by further including the pitch angle dependence (solid lines). (c) Simulated electron pitch angle distribution by including chorus-driven local acceleration only and (d) chorus-driven local acceleration and radial diffusion with (without) including the pitch angle dependence for radial diffusion coefficients indicated by the solid (dashed) lines.

simulation. The comparison of the dipole model and the TS04D model [*Tsyganenko and Sitnov,* 2005], as well as the observed magnetic field intensity, is shown in the supporting information Figure S5. In the premidnight and dusk sector along the satellite trajectory, the difference between the measured and the dipole magnetic field intensity was mostly within a factor of two at $L < 6$, indicating that the contribution of the adiabatic effect may be insignificant compared to the substantial electron PSD increases up to 4 orders of magnitude (Figure 2). Moreover, in our simulation we adopted 4 h averaged values for wave and plasma parameters, as well as the electron PSD at the outer boundary ($L = 6$) and at the lower energy boundary ($\mu = 80$ MeV/G), which might be inaccurate to simulate the actual electron evolution.

As a further confirmation, we performed a quantitative comparison on the observed and simulated electron pitch angle distributions at the end of the simulation period (20 March 2015/00 UT) at $L = 4.5$, near the location where the peak in electron fluxes was observed, as shown in Figure 7. The observed electrons (Figure 7a) exhibited a flat-top pitch angle distribution peaking over 50°–130° with a strong gradient toward the loss cone below ~50° or above 130°. For the effect of radial diffusion, we also evaluate the effect of pitch angle dependence in radial diffusion coefficients by adding a pitch angle-dependent factor

$$D_{LL}^{*} = D_{LL} \times \left( \frac{Q(y)}{180 D(y)} \right)^{2}$$

where $y$ is sine of pitch angle, and $Q(y)$ and $D(y)$ is the auxiliary function [*Schulz,* 1991; *Miyoshi et al.*, 2006]. Here $D_{LL}$ is the original radial diffusion coefficient (sum of electric and magnetic terms) from *Ozeke et al.* [2014], and $D_{LL}^{*}$ is the radial diffusion coefficient after incorporating the effect of pitch angle dependence. This equation indicates that radial diffusion coefficients for particles with 90° pitch angle are larger than those with smaller pitch angles. By including radial diffusion only ($D_{LL}$ (Ozeke)), the simulation results (Figure 7b) with (solid lines) or without (dashed lines) including the pitch angle dependence effect underestimated the observed electron PSD, and neither of them were able to produce the observed flat-top distribution. The inclusion of the pitch angle dependence effect led to little change in the electron PSD at 90° pitch angle (solid lines), but the peaks are considerably narrower compared to those without including the pitch angle dependence (dashed lines). The simulation result by including chorus-driven local acceleration alone (Figure 7c) was indeed able to reproduce this characteristic flat-top distribution, but the gradient seems to be too strong toward the loss cone compared to the observation. The combined effect of radial diffusion and local acceleration led to the simulation result (Figure 7d) that is remarkably consistent with the observed profile (Figure 7a). The pitch angle dependence in radial diffusion plays an insignificant role in the overall

evolution of the electron PSD driven by both chorus waves and radial diffusion at this location ($L = 4.5$), as demonstrated by the subtle difference in solid and dashed lines in Figure 7d. Note that the inclusion of the pitch angle dependence in radial diffusion led to insignificant changes in the simulation results in Figure 6, which show the electron flux evolution at pitch angles of 80°, where the effect of pitch angle dependence is very weak. Interestingly, by including radial diffusion in addition to the chorus-driven local acceleration, the simulated electron PSD at multiple MeV further increased, which is more consistent with the observation. It is worthwhile to note that an additional inclusion of the plasmaspheric hiss effect did not lead to any change in the simulation result, since the averaged hiss wave intensity was very weak at this location with $L = 4.5$ (Figure 5c). In conclusion, at this electron peak location, chorus plays an important role in accelerating electrons from hundreds of keV to multiple MeV, and radial diffusion potentially accelerates electrons to even higher energies depending on the radial gradient in electron PSD.

## 6. Summary and Discussion

We performed a 3-D diffusion simulation to evaluate the quantitative roles of radial diffusion, chorus, and plasmaspheric hiss during the biggest storm over the past decade that occurred on 17 March 2015. In this process, we adopted the best available various wave models to calculate diffusion coefficients, including the event-specific chorus wave intensity evolution on a global scale using the POES technique, the latest statistical hiss wave properties and intensity distributions, and two different empirical models for radial diffusion considering the effect of pitch angle dependence. The principle conclusions of this paper are listed below.

1. Chorus plays an important role in accelerating seed electrons to multiple MeV near the developing peak location and produces the characteristic flat-top pitch angle distributions.
2. Radial diffusion alone underestimates the observed electron acceleration and is unable to produce the rising peak at the right location, while it plays a significant role in redistributing electrons and potentially accelerates them to even higher energies. Radial diffusion including the effect of pitch angle dependence causes weaker diffusion at smaller pitch angles and leads to narrower peaks at around 90° pitch angle.
3. Plasmaspheric hiss provides important scattering losses for hundreds of keV electrons, but its effect on ultrarelativistic electrons ($>$1 MeV) is relatively slow.
4. The quantitative comparison between the observations and diffusion-based simulations clearly demonstrates that various physical processes, such as chorus-driven local acceleration, radial diffusion, and pitch angle scattering loss by plasmaspheric hiss and EMIC waves, are needed altogether to better explain the observed dynamical evolution of radiation belt electrons in different time and space for different electron energies.

It is important to note that the high-resolution measurements of electron pitch angle distributions over a broad range of electron energies from Van Allen Probes provide important insights into the underlying physics driving the observed electron dynamics. For example, the flat-top pitch angle distribution observed in association with the rapid electron acceleration, when chorus wave intensity was also strong, provides further confirmation of the dominant role of chorus waves that play in causing electron acceleration. The butterfly pitch angle distributions observed by Van Allen Probes at $L = 4.5$ on the nightside near the shock arrival during the 17 March 2015 geomagnetic storm (the left two panels in Figure 4 (bottom)) suggest that the drift-shell splitting effect [*Sibeck et al*., 1987; *West et al*., 1973] is probably dominant.

Different from solar wind conditions during typical rapid electron acceleration events, where IMF $B_z$ was mostly negative for a prolonged time [*Miyoshi and Kataoka,* 2005, 2008; *Miyoshi et al*., 2013; *Thorne et al*., 2013a; *Li et al*., 2014, 2015b], during this large geomagnetic storm IMF $B_z$ was strongly fluctuating around 0 starting from 18 March 2015 for several days, as shown in Figure 1b. Intensified interplanetary ULF fluctuations are shown to substantially enhance nightside convection and increase the occurrence of substorm activity [*Lyons et al*., 2009]. This is also probably why the overall chorus wave activity lasted long, although chorus wave intensity was not extremely strong ($<$ ~100 pT), in association with the electron acceleration to $>$ 5 MeV with a time delay of ~1.5 days compared to the acceleration of electrons up to ~ 1 MeV.

In the present paper, we adopted quasi-linear diffusion theory, which is the primary tool used to evaluate radiation belt electron dynamics caused by wave-particle interactions on a global scale, to simulate the dynamical evolution of electrons over a broad range of the radiation belts. Although the problem of whether quasi-linear theory can properly describe electron dynamics for the waves with large amplitudes and discrete

structures is still under active research [e.g., *Albert,* 2002; *Bortnik et al*., 2008; *Cattell et al*., 2008; *Tao et al*., 2012, 2014], during the recovery phase of this largest geomagnetic storm we reproduced most of the observed spatiotemporal evolution of radiation belt electron dynamics reasonably well using 3-D diffusion simulation. Moreover, the observed time delay between the electron acceleration at 1.8 and 6.3 MeV is ~ 1.5 days, which is much slower than the typical acceleration timescale by nonlinear wave-particle interaction [e.g., *Omura et al*., 2015]. Therefore, we suggest that even during this largest storm quasi-linear theory seems to be valid to capture the essential physics of electron acceleration. However, we cannot completely rule out the presence of the nonlinear wave-particle interactions, and further investigations will be needed to find the evidence and address their importance using unprecedented wave and particle data from multiple satellites and the state-of-the-art theory and modeling.

Finally, we discuss the limitations and possible improvements of the present study. As noted before, a dipole magnetic field was adopted to calculate diffusion coefficients in pitch angle, momentum, and their mixed terms in our global simulation for chorus and plasmaspheric hiss. However, *Orlova et al.* [2012] have demonstrated that using a realistic magnetic field model can potentially lead to a significant difference particularly at energies above ~1 MeV during geomagnetically disturbed periods. Although the inclusion of the nondipole magnetic field model in diffusion coefficient calculations is technically plausible, it is computationally very expensive to be incorporated in the global-scale simulation and is thus beyond the scope of the present study. Furthermore, in our simulation we adopted two different empirical radial diffusion coefficients (dependent on *Kp* and *L* shell); neither of which were evaluated inside and outside the plasmasphere separately, where the ULF wave properties could be vastly different. These empirical radial diffusion coefficients are also independent of electron energy, which may not be realistic and need a careful examination. In the future, more realistic and event-specific radial diffusion coefficients, when available, will be used to evaluate the quantitative role of radial diffusion during this big geomagnetic storm and/or other interesting events.

**Acknowledgments**

This work was supported by RBSP-ECT and EMFISIS funding provided by JHU/APL contract 967399 and 921647 under NASA's prime contract NAS5-01072. The analysis at UCLA was supported by AFOSR award FA9550-15-1-0158, NASA grants NNX15AI96G, NNX15AF61G, NNX11AR64G, NNX13AI61G, and NNX14AI18G, and the NSF grants AGS 1405054 and 1564510. We acknowledge the Van Allen Probes data from EMFISIS obtained from https://emfisis.physics.uiowa.edu/data/index, REPT and MagEIS data obtained from http://www.rbsp-ect.lanl.gov/data_pub/, and THEMIS wave data obtained from http://themis.ssl.berkeley.edu/themis-data/. We also acknowledge plasmapause location data from http://enarc.space.swri.edu/PTP/. Furthermore, we greatly appreciate the NOAA POES data obtained from http://satdat.ngdc.noaa.gov/sem/poes/data/ and the NOAA POES team for providing helpful advice. We also thank the World Data Center for Geomagnetism, Kyoto, for providing *SYM-H* and *AL* index (http://wdc.kugi.kyoto-u.ac.jp/aeasy/index.html) and the Space Physics Data Facility at the NASA Goddard Space Flight Center for providing the OMNI2 data (ftp://spdf.gsfc.nasa.gov/pub/data/omni/omni_cdaweb/). We also would like to thank Kyle Murphy and Anthony Chan for providing helpful discussions in this study.

## References

Albert, J. M. (2002), Nonlinear interaction of outer zone electrons with VLF waves, *Geopys. Res. Lett., 29*(8), 1275, doi:10.1029/2001GL013941.

Albert, J. M., N. P. Meredith, and R. B. Horne (2009), Three-dimensional diffusion simulation of outer radiation belt electrons during the 9 October 1990 magnetic storm, *J. Geophys. Res.*, *114*, A09214, doi:10.1029/2009JA014336.

Angelopoulos, V. (2008), The THEMIS Mission, *Space Sci. Rev.*, *141*(1–4), 5–34, doi:10.1007/s11214-008-9336-1.

Baker, D. N., and S. G. Kanekal (2008), Solar cycle changes, geomagnetic variations, and energetic particle properties in the inner magnetosphere, *J. Atmos. Sol. Terr. Phys.*, *70*, 195–206, doi:10.1016/j.jastp.2007.08.031.

Baker, D. N., et al. (2013), The Relativistic Electron-Proton Telescope (REPT) instrument on board the Radiation Belt Storm Probes (RBSP) spacecraft: Characterization of Earth's radiation belt high-energy particle populations, *Space Sci. Rev.*, *179*, 337–381, doi:10.1007/s11214-012-9950-9.

Baker, D. N., et al (2014), An impenetrable barrier to ultrarelativistic electrons in the Van Allen radiation belts, *Nature*, *515*, 531–534, doi:10.1038/nature13956.

Blake, J. B., W. A. Kolasinski, R. W. Fillius, and E. G. Mullen (1992), Injection of electrons and protons with energies of tens of MeV into $L < 3$ on 24 March 1991, *Geophys. Res. Lett.*, *19*, 821–824, doi:10.1029/92GL00624.

Blake, J. B., et al. (2013), The Magnetic Electron Ion Spectrometer (MagEIS) instruments aboard the Radiation Belt Storm Probes (RBSP) spacecraft, *Space Sci. Rev.*, *179*(1), 383–421, doi:10.1007/s11214-013-9991-8.

Blum, L. W., Q. Schiller, X. Li, R. Millan, A. Halford, and L. Woodger (2013), New conjunctive CubeSat and balloon measurements to quantify rapid energetic electron precipitation, *Geophys. Res. Lett.*, *40*, 5833–5837, doi:10.1002/2013GL058546.

Bortnik, J., R. M. Thorne, and U. S. Inan (2008), Nonlinear interaction of energetic electrons with large amplitude chorus, *Geophys. Res. Lett.*, *35*, L21102, doi:10.1029/2008GL035500.

Boyd, A. J., H. E. Spence, S. G. Claudepierre, J. F. Fennell, J. B. Blake, D. N. Baker, G. D. Reeves, and D. . L. Turner (2014), Quantifying the radiation belt seed population in the March 17, 2013 electron acceleration event, *Geophys. Res. Lett.*, *41*, 2275–2281, doi:10.1002/2014GL059626.

Brautigam, D. H., and J. M. Albert (2000), Radial diffusion analysis of outer radiation belt electrons during the October 9, 1990, magnetic storm, *J. Geophys. Res.*, *105*(A1), 291–309, doi:10.1029/1999JA900344.

Cattell, C., et al. (2008), Discovery of very large amplitude whistler-mode waves in Earth's radiation belts, *Geophys. Res. Lett.*, *35*, L01105, doi:10.1029/2007GL032009.

Chen, Y., G. D. Reeves, and R. H. W. Friedel (2007), The energization of relativistic electrons in the outer Van Allen radiation belt, *Nat. Phys.*, *3*, doi:10.1038/nphys655.

Cully, C. M., R. E. Ergun, K. Stevens, A. Nammari, and J. Westfall (2008), The THEMIS digital fields board, *Space Sci. Rev.*, *141*(1–4), 343–355, doi:10.1007/s11214-008-9417-1.

Dai, L., J. R. Wygant, C. A. Cattell, S. Thaller, K. Kersten, A. Breneman, X. Tang, R. H. Friedel, S. G. Claudepierre, and X. Tao (2014), Evidence for injection of relativistic electrons into the Earth's outer radiation belt via intense substorm electric fields, *Geophys. Res. Lett.*, *41*, 1133–1141, doi:10.1002/2014GL059228.

Evans, D. S., and M. S. Greer (2004), Polar Orbiting Environmental Satellite Space Environment Monitor-2: Instrument descriptions and archive data documentation, *NOAA Tech. Mem. 93*, version 1.4, Space Weather Predict. Cent., Boulder, Colo.

Fennell, J. F., S. G. Claudepierre, J. B. Blake, T. P. O'Brien, J. H. Clemmons, D. N. Baker, H. E. Spence, and G. D. Reeves (2015), Van Allen Probes show that the inner radiation zone contains no MeV electrons: ECT/MagEIS data, *Geophys. Res. Lett.*, *42*, 1283–1289, doi:10.1002/2014GL062874.

Fok, M.-C., R. B. Horne, N. P. Meredith, and S. A. Glauert (2008), Radiation Belt Environment model: Application to space weather nowcasting, *J. Geophys. Res.*, *113,* A03S08, doi:10.1029/2007JA012558.

Furuya, N., Y. Omura, and D. Summers (2008), Relativistic turning acceleration of radiation belt electrons by whistler mode chorus, *J. Geophys. Res.*, *113*, A04224, doi:10.1029/2007JA012478.

Glauert, S. A., R. B. Horne, and N. P. Meredith (2014), Three-dimensional electron radiation belt simulations using the BAS Radiation Belt Model with new diffusion models for chorus, plasmaspheric hiss, and lightning-generated whistlers, *J. Geophys. Res. Space Physics*, *119*, 268–289, doi:10.1002/2013JA019281.

Goldstein, J., M. F. Thomsen, and A. DeJong (2014), In situ signatures of residual plasmaspheric plumes: Observations and simulation, *J. Geophys. Res. Space Physics*, *119*, 4706–4722, doi:10.1002/2014JA019953.

Green, J. C. (2013), *MEPED Telescope Data Processing Algorithm Theoretical Basis Document*, Natl. Oceanic and Atmos. Admin. Space Environ. Cent, Boulder, Colo.

Green, J. C., and M. G. Kivelson (2004), Relativistic electrons in the outer radiation belt: Differentiating between acceleration mechanisms, *J. Geophys. Res.*, *109*, A03213, doi:10.1029/2003JA010153.

Horne, R. B., and R. M. Thorne (1998), Potential waves for relativistic electron scattering and stochastic acceleration during magnetic storms, *Geophys. Res. Lett.*, *25*(15), 3011–3014, doi:10.1029/98GL01002.

Horne, R. B., et al. (2005a), Wave acceleration of electrons in the Van Allen radiation belts, *Nature*, *437*, 227–230, doi:10.1038/nature03939.

Horne, R. B., R. M. Thorne, S. A. Glauert, J. M. Albert, N. P. Meredith, and R. R. Anderson (2005b), Timescale for radiation belt electron acceleration by whistler mode chorus waves, *J. Geophys. Res.*, *110*, A03225, doi:10.1029/2004JA010811.

Horne, R. B., R. M. Thorne, S. A. Glauert, N. P. Meredith, D. Pokhotelov, and O. Santolík (2007), Electron acceleration in the Van Allen radiation belts by fast magnetosonic waves, *Geophys. Res. Lett.*, *34*, L17107, doi:10.1029/2007GL030267.

Huang, C.-L., H. E. Spence, M. K. Hudson, and S. R. Elkington (2010), Modeling radiation belt radial diffusion in ULF wave fields: 2. Estimating rates of radial diffusion using combined MHD and particle codes, *J. Geophys. Res.*, *115*, A06216, doi:10.1029/2009JA014918.

Hudson, M. K., S. R. Elkington, J. G. Lyon, C. C. Goodrich, and T. J. Rosenberg (1999), Simulation of radiation belt dynamics driven by solar wind variations, in *Sun-Earth Plasma Connections*, edited by J. L. Burch, R. L. Carovillano, and S. K. Antiochos, AGU, Washington, D. C., doi:10.1029/GM109p0171.

Iles, R. H. A., N. P. Meredith, A. N. Fazakerley, and R. B. Horne (2006), Phase space density analysis of the outer radiation belt energetic electron dynamics, *J. Geophys. Res.*, *111*, A03204, doi:10.1029/2005JA011206.

Jaynes, A. N., et al. (2015), Source and seed populations for relativistic electrons: Their roles in radiation belt changes, *J. Geophys. Res. Space Physics*, *120*, 7240–7254, doi:10.1002/2015JA021234.

Jordanova, V. K., and Y. S. Miyoshi (2005), Relativistic model of ring current and radiation belt ions and electrons: Initial results, *Geophys. Res. Lett.*, *32*, L14104, doi:10.1029/2005GL023020.

Jordanova, V. K., J. Albert, and Y. Miyoshi (2008), Relativistic electron precipitation by EMIC waves from self-consistent global simulations, *J. Geophys. Res.*, *113*, A00A10, doi:10.1029/2008JA013239.

Kanekal, S. G., et al. (2015), Relativistic electron response to the combined magnetospheric impact of a coronal mass ejection overlapping with a high-speed stream: Van Allen Probes observations, *J. Geophys. Res. Space Physics*, *120*, 7629–7641, doi:10.1002/2015JA021395.

Kennel, C. F., and F. Engelmann (1966), Velocity space diffusion from weak plasma turbulence in a magnetic field, *Phys. Fluids*, *9*, 2377–2389, doi:10.1063/1.1761629.

Kim, H.-J., and A. A. Chan (1997), Fully adiabatic changes in storm time relativistic electron fluxes, *J. Geophys. Res.*, *102*(A10), 22,107–22,116, doi:10.1029/97JA01814.

Kim, K. C., D.-Y. Lee, H.-J. Kim, L. R. Lyons, E. S. Lee, M. K. Öztürk, and C. R. Choi (2008), Numerical calculations of relativistic electron drift loss effect, *J. Geophys. Res.*, *113*, A09212, doi:10.1029/2007JA013011.

Kletzing, C. A., et al. (2013), The Electric and Magnetic Field Instrument Suite and Integrated Science (EMFISIS) on RBSP, *Space Sci. Rev.*, *179*, 127–181, doi:10.1007/s11214-013-9993-6.

Kurth, W. S., S. De Pascuale, J. B. Faden, C. A. Kletzing, G. B. Hospodarsky, S. Thaller, and J. R. Wygant (2015), Electron densities inferred from plasma wave spectra obtained by the Waves instrument on Van Allen Probes, *J. Geophys. Res. Space Physics*, *120*, 904–914, doi:10.1002/2014JA020857.

Lenchek, A. M., S. F. Singer, and R. C. Wentworth (1961), Geomagnetically trapped electrons from cosmic ray albedo neutrons, *J. Geophys. Res.*, *66*(12), 4027–4046, doi:10.1029/JZ066i012p04027.

Li, J., et al. (2016), Formation of energetic electron butterfly distributions by magnetosonic waves via Landau resonance, *Geophys. Res. Lett.*, *43*, 3009–3016, doi:10.1002/2016GL067853.

Li, W., Y. Y. Shprits, and R. M. Thorne (2007), Dynamic evolution of energetic outer zone electrons due to wave-particle interactions during storms, *J. Geophys. Res.*, *112*, A10220, doi:10.1029/2007JA012368.

Li, W., R. M. Thorne, V. Angelopoulos, J. Bortnik, C. M. Cully, B. Ni, O. LeContel, A. Roux, U. Auster, and W. Magnes (2009), Global distribution of whistler-mode chorus waves observed on the THEMIS spacecraft, *Geophys. Res. Lett.*, *36*, L09104, doi:10.1029/2009GL037595.

Li, W., J. Bortnik, R. M. Thorne, and V. Angelopoulos (2011), Global distribution of wave amplitudes and wave normal angles of chorus waves using THEMIS wave observations, *J. Geophys. Res.*, *116*, A12205, doi:10.1029/2011JA017035.

Li, W., R. Thorne, J. Bortnik, R. McPherron, Y. Nishimura, V. Angelopoulos, and I. G. Richardson (2012), Evolution of chorus waves and their source electrons during storms driven by corotating interaction regions, *J. Geophys. Res.*, *117*, A08209, doi:10.1029/2012JA017797.

Li, W., B. Ni, R. M. Thorne, J. Bortnik, J. C. Green, C. A. Kletzing, W. S. Kurth, and G. B. Hospodarsky (2013), Constructing the global distribution of chorus wave intensity using measurements of electrons by the POES satellites and waves by the Van Allen Probes, *Geophys. Res. Lett.*, *40*, 4526–4532, doi:10.1002/grl.50920.

Li, W., et al. (2014), Radiation belt electron acceleration by chorus waves during the 17 March 2013 storm, *J. Geophys. Res. Space Physics*, *119*, 4681–4693, doi:10.1002/2014JA019945.

Li, W., Q. Ma, R. M. Thorne, J. Bortnik, C. A. Kletzing, W. S. Kurth, G. B. Hospodarsky, and Y. Nishimura (2015a), Statistical properties of plasmaspheric hiss derived from Van Allen Probes data and their effects on radiation belt electron dynamics, *J. Geophys. Res. Space Physics*, *120*, 3393–3405, doi:10.1002/2015JA021048.

Li, W., R. M. Thorne, J. Bortnik, D. N. Baker, G. D. Reeves, S. G. Kanekal, H. E. Spence, and J. C. Green (2015b), Solar wind conditions leading to efficient radiation belt electron acceleration: A superposed epoch analysis, *Geophys. Res. Lett.*, *42*, 6906–6915, doi:10.1002/2015GL065342.

Li, X., I. Roth, M. Temerin, J. R. Wygant, M. K. Hudson, and J. B. Blake (1993), Simulation of the prompt energization and transport of radiation belt particles during the March 24, 1991 SSC, *Geophys. Res. Lett.*, *20*, 2423–2426, doi:10.1029/93GL02701.

Lyons, L. R., et al. (2009), Evidence that solar wind fluctuations substantially affect global convection and substorm occurrence, *J. Geophys. Res.*, *114*, A11306, doi:10.1029/2009JA014281.
Ma, Q., et al. (2015), Modeling inward diffusion and slow decay of energetic electrons in the Earth's outer radiation belt, *Geophys. Res. Lett.*, *42*, 987–995, doi:10.1002/2014GL062977.
Ma, Q., W. Li, R. M. Thorne, J. Bortnik, C. A. Kletzing, W. S. Kurth, and G. B. Hospodarsky (2016), Electron scattering by magnetosonic waves in the inner magnetosphere, *J. Geophys. Res. Space Physics*, *121*, 274–285, doi:10.1002/2015JA021992.
Mathie, R. A., and I. R. Mann (2000), A correlation between extended intervals of ULF wave power and storm-time geosynchronous relativistic electron flux enhancements, *Geophys. Res. Lett.*, *27*, 3261–3264, doi:10.1029/2000GL003822.
Matsumura, C., Y. Miyoshi, K. Seki, S. Saito, V. Angelopoulos, and J. Koller (2011), Outer radiation belt boundary location relative to the magnetopause: Implications for magnetopause shadowing, *J. Geophys. Res.*, *116*, A06212, doi:10.1029/2011JA016575.
Mauk, B. H., N. J. Fox, S. G. Kanekal, R. L. Kessel, D. G. Sibeck, and A. Ukhorskiy (2013), Science objectives and rationale for the Radiation Belt Storm Probes mission, *Space Sci. Rev.*, *179*(1), 3–27, doi:10.1007/s11214-012-9908-y.
McPherron, R. L., D. N. Baker, and N. U. Crooker (2009), Role of the Russell-McPherron effect in the acceleration of relativistic electrons, *J. Atmos. Sol. Terr. Phys.*, *71*, 1032–1044, doi:10.1016/j.jastp.2008.11.002.
Meredith, N. P., R. B. Horne, S. A. Glauert, R. M. Thorne, D. Summers, J. M. Albert, and R. R. Anderson (2006), Energetic outer zone electron loss timescales during low geomagnetic activity, *J. Geophys. Res.*, *111*, A05212, doi:10.1029/2005JA011516.
Meredith, N. P., R. B. Horne, S. A. Glauert, and R. R. Anderson (2007), Slot region electron loss timescales due to plasmaspheric hiss and lightning-generated whistlers, *J. Geophys. Res.*, *112*, A08214, doi:10.1029/2007JA012413.
Meredith, N. P., R. B. Horne, A. Sicard-Piet, D. Boscher, K. H. Yearby, W. Li, and R. M. Thorne (2012), Global model of lower band and upper band chorus from multiple satellite observations, *J. Geophys. Res.*, *117*, A10225, doi:10.1029/2012JA017978.
Millan, R. M., and R. M. Thorne (2007), Review of radiation belt relativistic electron loss, *J. Atmos. Sol. Terr. Phys.*, *69*, 362–377, doi:10.1016/j.jastp.2006.06.019.
Miyoshi, Y., and R. Kataoka (2005), Ring current ions and radiation belt electrons during geomagnetic storms driven by coronal mass ejections and corotating interaction regions, *Geophys. Res. Lett.*, *32*, L21105, doi:10.1029/2005GL024590.
Miyoshi, Y., and R. Kataoka (2008), Flux enhancement of the outer radiation belt electrons after the arrival of stream interaction regions, *J. Geophys. Res.*, *113*, A03S09, doi:10.1029/2007JA012506.
Miyoshi, Y. S., V. K. Jordanova, A. Morioka, M. F. Thomsen, G. D. Reeves, D. S. Evans, and J. C. Green (2006), Observations and modeling of energetic electron dynamics during the October 2001 storm, *J. Geophys. Res.*, *111*, A11S02, doi:10.1029/2005JA011351.
Miyoshi, Y., A. Morioka, T. Obara, H. Misawa, T. Nagai, and Y. Kasahara (2003), Rebuilding process of the outer radiation belt during the 3 November 1993 magnetic storm: NOAA and Exos-D observations, *J. Geophys. Res.*, *108*(A1), 1004, doi:10.1029/2001JA007542.
Miyoshi, Y., K. Sakaguchi, K. Shiokawa, D. Evans, J. Albert, M. Connors, and V. Jordanova (2008), Precipitation of radiation belt electrons by EMIC waves, observed from ground and space, *Geophys. Res. Lett.*, *35*, L23101, doi:10.1029/2008GL035727.
Miyoshi, Y., R. Kataoka, Y. Kasahara, A. Kumamoto, T. Nagai, and M. F. Thomsen (2013), High-speed solar wind with southward interplanetary magnetic field causes relativistic electron flux enhancement of the outer radiation belt via enhanced condition of whistler waves, *Geophys. Res. Lett.*, *40*, 4520–4525, doi:10.1002/grl.50916.
Ni, B., R. M. Thorne, Y. Y. Shprits, and J. Bortnik (2008), Resonant scattering of plasma sheet electrons by whistler-mode chorus: Contribution to diffuse auroral precipitation, *Geophys. Res. Lett.*, *35*, L11106, doi:10.1029/2008GL034032.
Ni, B., J. Bortnik, R. M. Thorne, Q. Ma, and L. Chen (2013), Resonant scattering and resultant pitch angle evolution of relativistic electrons by plasmaspheric hiss, *J. Geophys. Res. Space Physics*, *118*, 7740–7751, doi:10.1002/2013JA019260.
Ni, B., W. Li, R. M. Thorne, J. Bortnik, J. C. Green, C. A. Kletzing, W. S. Kurth, G. B. Hospodarsky, and M. de Soria-Santacruz Pich (2014), A novel technique to construct the global distribution of whistler mode chorus wave intensity using low-altitude POES electron data, *J. Geophys. Res. Space Physics*, *119*, 5685–5699, doi:10.1002/2014JA019935.
Ohtani, S., Y. Miyoshi, H. J. Singer, and J. M. Weygand (2009), On the loss of relativistic electrons at geosynchronous altitude: Its dependence on magnetic configurations and external conditions, *J. Geophys. Res.*, *114*, A01202, doi:10.1029/2008JA013391.
Omura, Y., and Q. Zhao (2013), Relativistic electron microbursts due to nonlinear pitch angle scattering by EMIC triggered emissions, *J. Geophys. Res. Space Physics*, *118*, 5008–5020, doi:10.1002/jgra.50477.
Omura, Y., Y. Miyashita, M. Yoshikawa, D. Summers, M. Hikishima, Y. Ebihara, and Y. Kubota (2015), Formation process of relativistic electron flux through interaction with chorus emissions in the Earth's inner magnetosphere, *J. Geophys. Res. Space Physics*, *120*, 9545–9562, doi:10.1002/2015JA021563.
Orlova, K. G., Y. Y. Shprits, and B. Ni (2012), Bounce-averaged diffusion coefficients due to resonant interaction of the outer radiation belt electrons with oblique chorus waves computed in a realistic magnetic field model, *J. Geophys. Res.*, *117*, A07209, doi:10.1029/2012JA017591.
Ozeke, L. G., I. R. Mann, K. R. Murphy, I. Jonathan Rae, and D. K. Milling (2014), Analytic expressions for ULF wave radiation belt radial diffusion coefficients, *J. Geophys. Res. Space Physics*, *119*, 1587–1605, doi:10.1002/2013JA019204.
Perry, K. L., M. K. Hudson, and S. R. Elkington (2005), Incorporating spectral characteristics of Pc5 waves into three-dimensional radiation belt modeling and the diffusion of relativistic electrons, *J. Geophys. Res.*, *110*, A03215, doi:10.1029/2004JA010760.
Reeves, G. D., K. L. McAdams, R. H. W. Friedel, and T. P. O'Brien (2003), Acceleration and loss of relativistic electrons during geomagnetic storms, *Geophys. Res. Lett.*, *30*(10), 1529, doi:10.1029/2002GL016513.
Reeves, G. D., et al. (2013), Electron acceleration in the heart of the Van Allen radiation belts, *Science*, *341*(6149), 991–994, doi:10.1126/science.1237743.
Reeves, G. D., et al. (2015), Energy-dependent dynamics of keV to MeV electrons in the inner zone, outer zone, and slot regions, *J. Geophys. Res. Space Physics*, *121*, 397–412, doi:10.1002/2015JA021569.
Saito, S., Y. Miyoshi, and K. Seki (2010), A split in the outer radiation belt by magnetopause shadowing: Test particle simulations, *J. Geophys. Res.*, *115*, A08210, doi:10.1029/2009JA014738.
Santolík, O., D. A. Gurnett, J. S. Pickett, M. Parrot, and N. Cornilleau-Wehrlin (2003), Spatio-temporal structure of storm-time chorus, *J. Geophys. Res.*, *108*(A7), 1278, doi:10.1029/2002JA009791.
Schulz, M. (1991), The magnetosphere, in *Geomagnetism*, vol. 4, edited by J. A. Jacobs, pp. 87–293, Elsevier, New York.
Schulz, M., and L. J. Lanzerotti (1974), *Particle Diffusion in the Radiation Belts*, Springer, New York, doi:10.1007/978-3-642-65675-0.
Sheeley, B. W., M. B. Moldwin, H. K. Rassoul, and R. R. Anderson (2001), An empirical plasmasphere and trough density model: CRRES observations, *J. Geophys. Res.*, *106*(A11), 25,631–25,641, doi:10.1029/2000JA000286.
Shprits, Y. Y., R. M. Thorne, R. Friedel, G. D. Reeves, J. Fennell, D. N. Baker, and S. G. Kanekal (2006), Outward radial diffusion driven by losses at magnetopause, *J. Geophys. Res.*, *111*, A11214, doi:10.1029/2006JA011657.

Shprits, Y. Y., D. Subbotin, and B. Ni (2009), Evolution of electron fluxes in the outer radiation belt computed with the VERB code, *J. Geophys. Res.*, *114*, A11209, doi:10.1029/2008JA013784.

Shprits, Y. Y., A. Kellerman, A. Drozdov, H. Spense, G. Reeves, and D. Baker (2015), Combined convective and diffusive simulations: VERB-4D comparison with March 17, 2013 Van Allen Probes observations, *Geophys. Res. Lett.*, *42*, 9600–9608, doi:10.1002/2015GL065230.

Shue, J. H., et al. (1998), Magnetopause location under extreme solar wind conditions, *J. Geophys. Res.*, *103*(A8), 17, 691–17,700, doi:10.1029/98JA01103.

Sibeck, D. G., R. W. McEntire, A. T. Y. Lui, R. E. Lopez, and S. M. Krimigis (1987), Magnetic field drift shell splitting: Cause of unusual dayside particle pitch angle distributions during storms and substorms, *J. Geophys. Res.*, *92*(A12), 13,485–13,497, doi:10.1029/JA092iA12p13485.

Spence, H. E., et al. (2013), Science Goals and Overview of the Energetic Particle, Composition, and Thermal Plasma (ECT) Suite on NASA's Radiation Belt Storm Probes (RBSP) mission, *Space Sci. Rev.*, *179*(1), 311–336, doi:10.1007/s11214-013-0007-5.

Su, Z., et al. (2015), Ultra-low-frequency wave-driven diffusion of radiation belt relativistic electrons, *Nat. Commun.*, *6*, 10096, doi:10.1038/ncomms10096.

Summers, D., and R. M. Thorne (2003), Relativistic electron pitch-angle scattering by electromagnetic ion cyclotron waves during geomagnetic storms, *J. Geophys. Res.*, *108*(A4), 1143, doi:10.1029/2002JA009489.

Summers, D., C. Ma, N. P. Meredith, R. B. Horne, R. M. Thorne, D. Heynderickx, and R. R. Anderson (2002), Model of the energization of outer-zone electrons by whistler-mode chorus during the October 9, 1990 geomagnetic storm, *Geophys. Res. Lett.*, *29*(24), 2174, doi:10.1029/2002GL016039.

Tao, X., J. Bortnik, J. M. Albert, K. Liu, and R. M. Thorne (2011), Comparison of quasilinear diffusion coefficients for parallel propagating whistler mode waves with test particle simulations, *Geophys. Res. Lett.*, *38*, L06105, doi:10.1029/2011GL046787.

Tao, X., J. Bortnik, J. M. Albert, and R. M. Thorne (2012), Comparison of bounce-averaged quasi-linear diffusion coefficients for parallel propagating whistler mode waves with test particle simulations, *J. Geophys. Res.*, *117*, A10205, doi:10.1029/2012JA017931.

Tao, X., J. Bortnik, J. M. Albert, R. M. Thorne, and W. Li (2014), Effects of discreteness of chorus waves on quasilinear diffusion-based modeling of energetic electron dynamics, *J. Geophys. Res. Space Physics*, *119*, 8848–8857, doi:10.1002/2014JA020022.

Thorne, R. M. (2010), Radiation belt dynamics: The importance of wave-particle interactions, *Geophys. Res. Lett.*, *37*, L22107, doi:10.1029/2010GL044990.

Thorne, R. M., and C. F. Kennel (1971), Relativistic electron precipitation during magnetic storm main phase, *J. Geophys. Res.*, *76*(19), 4446–4453, doi:10.1029/JA076i019p04446.

Thorne, R. M., et al. (2013a), Rapid local acceleration of relativistic radiation belt electrons by magnetospheric chorus, *Nature*, *504*, 411–414, doi:10.1038/nature12889.

Thorne, R. M., et al. (2013b), Evolution and slow decay of an unusual narrow ring of relativistic electrons near $L \sim 3.2$ following the September 2012 magnetic storm, *Geophys. Res. Lett.*, *40*, 3507–3511, doi:10.1002/grl.50627.

Tsurutani, B. T., and E. J. Smith (1977), Two types of magnetospheric ELF chorus and their substorm dependences, *J. Geophys. Res.*, *82*(32), 5112–5128, doi:10.1029/JA082i032p05112.

Tsyganenko, N. A. (1989), A magnetospheric magnetic field model with a warped tail current sheet, *Planet. Space Sci.*, *37*, 5–20, doi:10.1016/0032-0633(89)90066-4.

Tsyganenko, N. A., and M. I. Sitnov (2005), Modeling the dynamics of the inner magnetosphere during strong geomagnetic storms, *J. Geophys. Res.*, *110*, A03208, doi:10.1029/2004JA010798.

Tu, W., S. R. Elkington, X. Li, W. Liu, and J. Bonnell (2012), Quantifying radial diffusion coefficients of radiation belt electrons based on global MHD simulation and spacecraft measurements, *J. Geophys. Res.*, *117*, A10210, doi:10.1029/2012JA017901.

Tu, W., G. S. Cunningham, Y. Chen, S. K. Morley, G. D. Reeves, J. B. Blake, D. N. Baker, and H. Spence (2014), Event-specific chorus wave and electron seed population models in DREAM3D using the Van Allen Probes, *Geophys. Res. Lett.*, *41*, 1359–1366, doi:10.1002/2013GL058819.

Turner, D. L., Y. Shprits, M. Hartinger, and V. Angelopoulos (2012), Explaining sudden losses of outer radiation belt electrons during geomagnetic storms, *Nat. Phys.*, *8*, 208–212, doi:10.1038/NPHYS2185.

Turner, D. L., et al. (2014), Competing source and loss mechanism due to wave-particle interactions in Earth's outer radiation belt during the 30 Sep.–03 Oct. 2012 geomagnetic storm, *J. Geophys. Res. Space Physics*, *119*, 1960–1979, doi:10.1002/2014JA019770.

Ukhorskiy, A. Y., M. I. Sitnov, K. Takahashi, and B. J. Anderson (2009), Radial transport of radiation belt electrons due to stormtime Pc5 waves, *Ann. Geophys.*, *27*, 2173–2181, doi:10.5194/angeo-27-2173-2009.

Ukhorskiy, A. Y., M. I. Sitnov, R. M. Millan, and B. T. Kress (2011), The role of drift orbit bifurcations in energization and loss of electrons in the outer radiation belt, *J. Geophys. Res.*, *116*, A09208, doi:10.1029/2011JA016623.

Ukhorskiy, A. Y., M. I. Sitnov, R. M. Millan, B. T. Kress, J. F. Fennell, S. G. Claudepierre, and R. J. Barnes (2015), Global storm time depletion of the outer electron belt, *J. Geophys. Res. Space Physics*, *120*, 2543–2556, doi:10.1002/2014JA020645.

Usanova, M. E., et al. (2014), Effect of EMIC waves on relativistic and ultrarelativistic electron populations: Ground-based and Van Allen Probes observations, *Geophys. Res. Lett.*, *41*, 1375–1381, doi:10.1002/2013GL059024.

Van Allen, J. A. (1959), The geomagnetically trapped corpuscular radiation, *J. Geophys. Res.*, *64*, 1683–1689, doi:10.1029/JZ064i011p01683.

West, H. I., Jr., R. M. Buck, and J. R. Walton (1973), Electron pitch angle distributions throughout the magnetosphere as observed on Ogo 5, *J. Geophys. Res.*, *78*(7), 1064–1081, doi:10.1029/JA078i007p01064.

Xiao, F., C. Yang, Z. Su, Q. Zhou, Z. He, Y. He, D. N. Baker, H. E. Spence, H. O. Funsten, and J. B. Blake (2015), Wave-driven butterfly distribution of Van Allen belt relativistic electrons, *Nat. Commun.*, *6*, 8590, doi:10.1038/ncomms9590.

Zheng, L., A. A. Chan, J. M. Albert, S. R. Elkington, J. Koller, R. B. Horne, S. A. Glauert, and N. . P. Meredith (2014), Three-dimensional stochastic modeling of radiation belts in adiabatic invariant coordinates, *J. Geophys. Res. Space Physics*, *119*, 7615–7635, doi:10.1002/2014JA020127.